

PROCEEDINGS OF SPIE

[SPIDigitalLibrary.org/conference-proceedings-of-spie](https://spiedigitallibrary.org/conference-proceedings-of-spie)

Testbed demonstration of high-contrast coronagraph imaging in search for Earth-like exoplanets

Seo, Byoung-Joon, Patterson, Keith, Balasubramanian, Kunjithapatham, Crill, Brendan, Chui, Talso, et al.

Byoung-Joon Seo, Keith Patterson, Kunjithapatham Balasubramanian, Brendan Crill, Talso Chui, Daniel Echeverri, Brian Kern, David Marx, Dwight Moody, Camilo Mejia Prada, Garreth Ruane, Fang Shi, John Shaw, Nick Siegler, Hong Tang, John Trauger, Daniel Wilson, Robert Zimmer, "Testbed demonstration of high-contrast coronagraph imaging in search for Earth-like exoplanets," Proc. SPIE 11117, Techniques and Instrumentation for Detection of Exoplanets IX, 111171V (16 September 2019); doi: 10.1117/12.2530033

SPIE.

Event: SPIE Optical Engineering + Applications, 2019, San Diego, California, United States

Testbed demonstration of high-contrast coronagraph imaging in search for Earth-like exoplanets

Byoung-Joon Seo^a, Keith Patterson^a, Kunjithapatham Balasubramanian^a, Brendan Crill^a, Talso Chui^a, Daniel Echeverri^b, Brian Kern^a, David Marx^a, Dwight Moody^a, Camilo Mejia Prada^a, Garreth Ruane^a, Fang Shi^a, John Shaw^a, Nick Siegler^a, Hong Tang^a, John Trauger^a, Daniel Wilson^a and Robert Zimmer^a

^a Jet Propulsion Laboratory, California Institute of Technology, 4800 Oak Grove Dr., Pasadena, CA. 91109, USA

^b Department of Astronomy, California Institute of Technology, 1200 E. California Blvd., Pasadena, CA. 91125, USA

ABSTRACT

Direct imaging of an Earth-like exoplanet requires starlight suppression with a contrast ratio on the order of 1×10^{-10} at small angular separations of 100 milliarcseconds or less in visible light with more than 50 nm bandwidth. To our knowledge, the technology needed to achieve the contrast and stability has not been demonstrated as of January 2019. The science requirements for near future National Aeronautics and Space Administration (NASA) missions such as James Webb Space Telescope (JWST)'s Near Infrared Camera (NIRCam) coronagraph and Wide-Field InfraRed Survey Telescope (WFIRST) Coronagraph Instrument (CGI) are at least 10 times short. To investigate and guide the technology to reach this capability, we built a high contrast coronagraph testbed at NASA's Jet Propulsion Laboratory (JPL). Titled the Decadal Survey Testbed (DST), this state-of-art testbed is based on the accumulated experience of JPL's High Contrast Imaging Testbed (HCIT) team. Currently, the DST hosts a Hybrid Lyot Coronagraph (HLC) with an unobscured, circular pupil. The DST also has two deformable mirrors and is equipped with the Low Order Wavefront Sensing and Control (LOWFS/C) subsystem to sense and correct the dynamic wavefront disturbances. In this paper, we present up-to-date progress of the testbed demonstration. As of January 2019, we repeatedly obtain convergence below 4×10^{-10} mean contrast with 10% broadband light centered at 550 nm in a 360 degrees dark hole with a working angle between $3 \lambda/D$ and $8 \lambda/D$. We show the key elements used in the testbed and the performance results with associated analysis.

Keywords: instrumentation, exoplanets, direct detection, coronagraphs

*Address all correspondence to Byoung-Joon Seo, Email: Byoung-Joon.Seo@jpl.nasa.gov

1. INTRODUCTION

The goals of National Aeronautics and Space Administration (NASA)'s next generation space coronagraph missions are aligned with search for habitable Earth-like exoplanets and their direct imaging. Achieving this goal requires not only a large aperture telescope such as Large UV/Optical/IR Surveyor (LUVOIR) and Habitable Exoplanet Observatory (HabEx),^{1,2} but also a high performance coronagraph instrument.

Direct imaging of an Earth-like exoplanet requires starlight suppression with a contrast ratio on the order of 1×10^{-10} at small angular separations of 100 milliarcseconds or less in visible light with more than 50 nm bandwidth. Such high coronagraph performance can be obtained by several key technological improvement including stable Deformable Mirror (DM), optimized coronagraph design, sensitive detectors, mechanical and thermal stability, and advanced wavefront control algorithm. To our knowledge, the technology needed to achieve the contrast and stability has not been demonstrated as of January 2019. The science requirements for near future National Aeronautics and Space Administration (NASA) missions such as James Webb Space Telescope (JWST)'s Near Infrared Camera (NIRCam) coronagraph and Wide-Field InfraRed Survey Telescope (WFIRST) Coronagraph Instrument (CGI) are at least 10 times short.³

©2019 California Institute of Technology. Government sponsorship acknowledged.

Techniques and Instrumentation for Detection of Exoplanets IX, edited by Stuart B. Shaklan, Proc. of SPIE Vol. 11117, 111171V · © 2019 SPIE · CCC code: 0277-786X/19/\$21 · doi: 10.1117/12.2530033

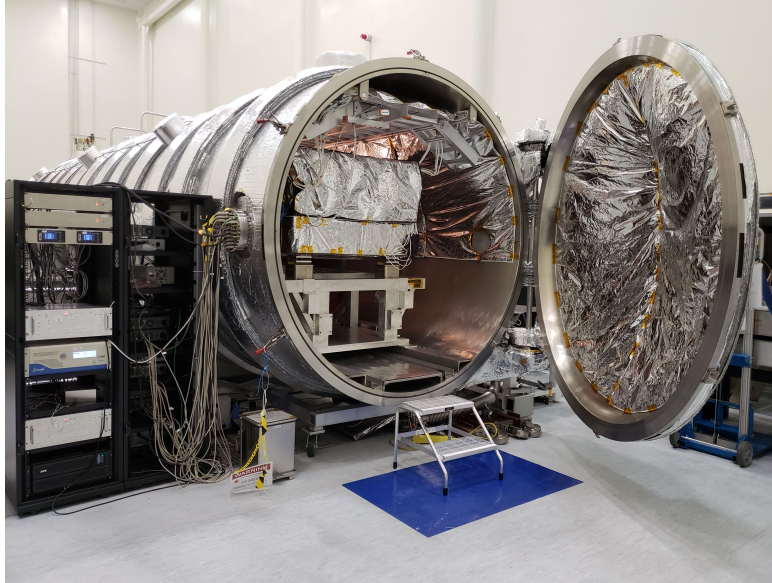


Figure 1. Photo of the DST when it is inside the vacuum chamber in JPL's HCIT.

To investigate and guide the technology to reach this capability, we, NASA's Exoplanet Exploration Program (ExEP) office, built a high contrast coronagraph testbed at NASA's Jet Propulsion Laboratory (JPL). Titled the Decadal Survey Testbed (DST), this state-of-art testbed is based on the accumulated experience of JPL's High Contrast Imaging Testbed (HCIT) team. As of January 2019, the DST is configured as its early stage (Phase A) hosting a Lyot coronagraph as its coronagraph architecture with an unobscured, circular pupil. The DST also has two DMs and is equipped with the Low Order Wavefront Sensing and Control (LOWFS/C) subsystem to sense and correct the dynamic wavefront disturbances.

We present up-to-date progress of the testbed demonstration in this paper. We repeatedly obtain convergence below 4×10^{-10} mean contrast with 10 % broadband light centered at 550 nm in a 360 degrees dark hole with a working angle between $3 \lambda/D$ and $8 \lambda/D$.

The remainder of this paper is structured as follows. Sec. 2 includes very brief overview of DST and refers its detail to our companion paper.⁴ Sec. 3 demonstrates the raw high contrast we have achieved in DST. Then, we discuss the breakdown of the contrast in Sec. 4 by showing itemized contrasts with necessary experiments and analysis. Future space telescopes with high contrast imaging instruments make use of a post processing technique to maximize visibility of the exoplanets. In Sec. 5, we apply a simple post processing algorithm, Angular Differential Imaging (ADI) technique, to the data measured from the testbed. Then, we estimate the practical planet identification capability. Finally, we conclude in Sec. 6 listing our future works.

2. TESTBED DESIGN

We refer to our companion paper by Patterson, et.al.⁴ on detail design description of DST. We only provide its brief description here. Fig. 1 is a photo of DST when it is inside the vacuum chamber in JPL's HCIT. As shown in the testbed layout in Fig. 2, DST is configured as Lyot coronagraph based on historical testbed performance in contrast levels.^{5,6} The optical prescription is similar to earlier HLC coronagraph testbeds in HCIT.^{6,7} One distinguishing feature of DST is that it only uses 6 Off Axis Parabolas (OAPs) with no flat fold mirrors to reduce the number of optics in the system, thus, making DST have a very simple optical layout and superior thermal and mechanical stability.⁴

3. HIGH CONTRAST DEMONSTRATION

Fig. 3 shows the raw high contrast image achieved after Wavefront Control (WFC) in DST. The averaged raw contrast is 3.82×10^{-10} with 10 % broadband light centered at 550 nm in the 360 degrees dark hole with working

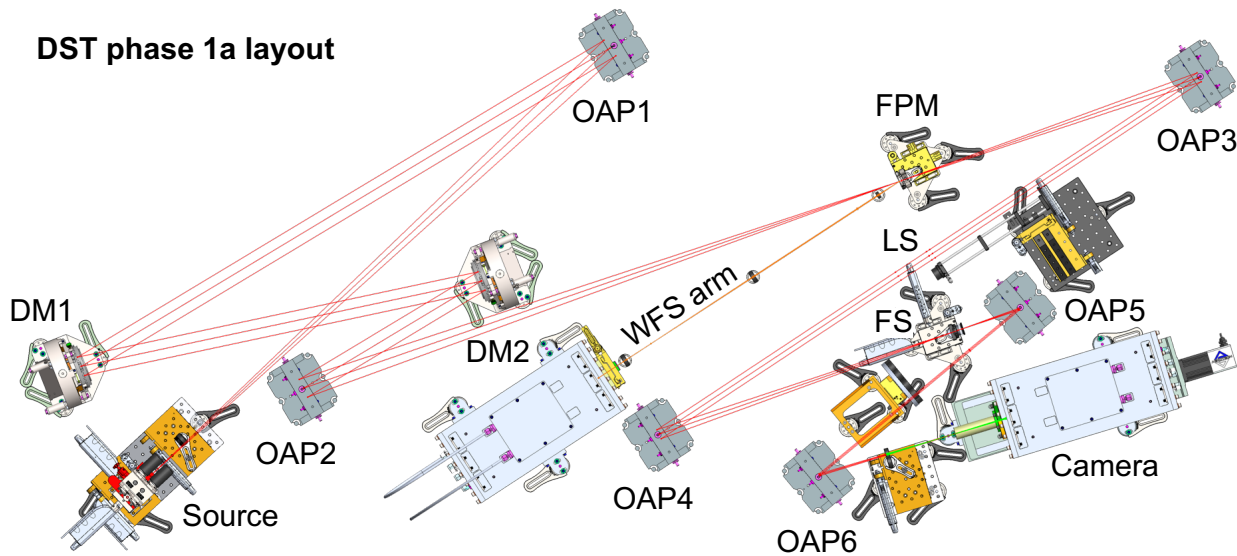


Figure 2. CAD layout of the Decadal Survey Testbed (DST) during commissioning in a Lyot coronagraph architecture. The optical prescription is similar to earlier HLC coronagraph testbeds in HCIT.^{6,7} One distinguishing feature of DST is that it only uses 6 OAPs with no flat fold mirrors to reduce the number of optics in the system, thus, making DST have a very simple optical layout and superior thermal and mechanical stability.⁴

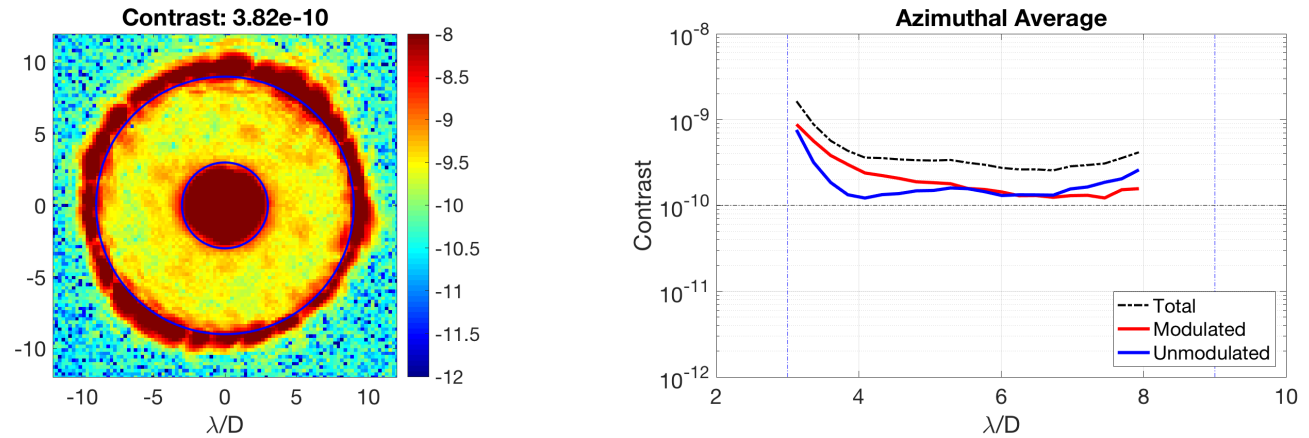


Figure 3. The raw high contrast image achieved in DST and its azimuthal average. The averaged raw contrast is 3.82×10^{-10} with 10% broadband light centered at 550 nm in the 360 degrees dark hole with working angle between $3 \lambda/D$ and $8 \lambda/D$. See text for more detail.

angle between $3 \lambda/D$ and $8 \lambda/D$. This is the 5 spectral bands' average centered at 528 nm, 531 nm, 550 nm, 561 nm and 572 nm with each band of 11 nm (or 2%) bandwidth respectively. The contrast measurement error is estimated to be less than 5%, which is dominated by a photometry estimation error.

The contrast is measured with linearly polarized light at the source and a linear polarization analyzer in the collimated space before the last OAP (between OAP5 and OAP6 in Fig. 2). As a Focal Plane Mask (FPM), we use a 100 nm thick simple bare Nickel occulter (on 3 nm thick titanium layer) with 98 μm diameter on the 6.25 mm thick fused silica (CVI Laser Optics, <https://www.cvilaseroptics.com/>) substrate with rear surface Anti-Reflection (AR) coated.

The obtained total contrast shown in Fig. 3 can be decomposed and itemized into multiple contributing components as in Table 1.

When we estimate the normalized complex electric field in the dark hole region, we employ the pairwise estimation scheme⁸ for this electric field estimation process. In this method, “probes” are placed on one of the DMs to modulate the complex electric field across the region of interest. The probes are applied typically in \pm pairs, providing the largest phase diversity and probe simplicity as well as minimizing DM gain uncertainty impact. Given images corresponding to several probe pairs, along with an image with no probes applied at all, we can retrieve the complex electric field at the region of interest. Unlike the phase retrieval algorithm, no mechanical motion is required except DM actuators. We describe our specific use of pairwise estimation process in detail in [7]. In addition to the complex electric field of the residual starlight in the dark hole, our pairwise estimation algorithm^{7,8} also can find a portion of light that does not interact with the applied probes. We refer to this light as “unmodulated” light. As the counterpart to the unmodulated light, we refer to the complex electric field of the residual starlight that responds to the probes as the “modulated” light. We refer [7] for definitions of “unmodulated” and “modulated” lights in more detail.

Accordingly, the inset figures in Fig. 1 shows that the total residual contrast is decomposed into the unmodulated light of 2.01×10^{-10} and modulated light of 1.82×10^{-10} . The black dot, blue, and red curves in the azimuthal average plot of Fig. 3 denote the total, modulated, and unmodulated light, respectively.

We identify two major contributions for the modulated light: the DM actuator Least Significant Bit (LSB) effect and chromatic control residual. On the other hand, the unmodulated light consists of three components: the occulter ghost effect, the testbed Line of Sight (LoS) jitter residual effect, and “unknown” component. In the following section of Sec. 4, we describe each value in more detail.

4. HIGH CONTRAST ANALYSIS

Fig. 4 shows the achieved contrasts in various different conditions in earlier testbed configuration where the BK7 material is used instead of fused silica for the FPM substrate. Fig. 4(a), (b) and (c) are the contrast images with 10 %, 6 % and narrow bandwidth, respectively. For 10 % bandwidth, we use the 5 spectral bands’ average centered at 528 nm, 539 nm, 550 nm, 561 nm and 572 nm with each band of 11 nm (or 2 %) bandwidth respectively. For 6 % bandwidth, we use the 3 spectral bands’ average centered at 539 nm, 550 nm, and 572 nm with each band of 11 nm (or 2 %) bandwidth respectively. We use the broadband laser system (SuperK Extreme, NKT Photonics) with the tunable spectral filter (SuperK Varia, NKT Photonics) except for the monochromatic

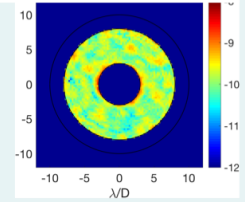
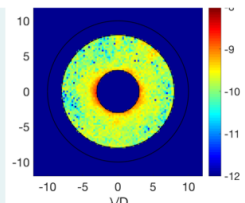
Contrast, 3.82E-10 Total		Measured	Model/Indirect Expectation	Morphology
Modulated 1.81E-10 	LSB effect of DM actuators	8.78E-11	~1E-10	Specklish
	Chromatic Control Residual	9.32E-11	~4E-11	Specklish
Unmodulated 2.01E-10 	Occluter Ghost (+Chromatic Residual)	1.01E-10	~1E-10	Patterned March with wavelength
	Testbed LoS Jitter impact	4.19E-11	< 1E-11	Centered
	Unknown	5.04E-11	N/A	Diffused

Table 1. The obtained total contrast of 3.82×10^{-10} shown in Fig. 3 can be decomposed into multiple contribution components.

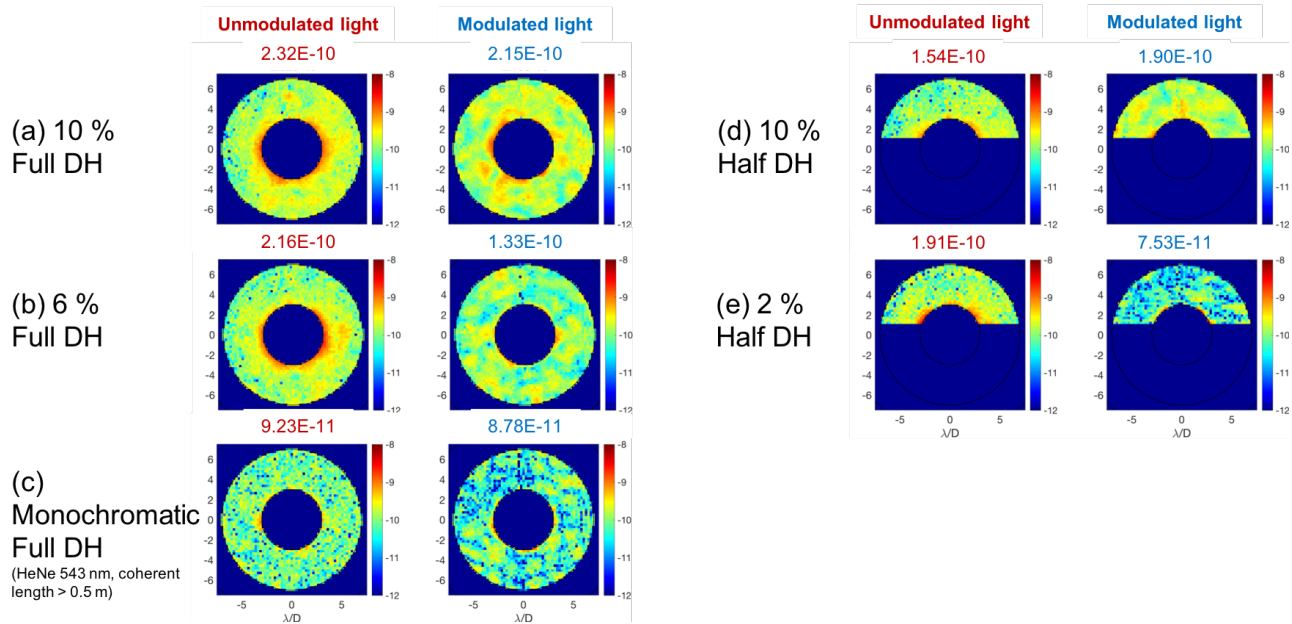


Figure 4. The achieved contrasts in various different conditions in earlier testbed configuration where the BK7 material is used instead of fused silica for the FPM substrate. Based on this result, we can deduce and itemize some of contrast contributions in the measured column of Table 1.

light. For the monochromatic light, we use the HeNe 543 nm with narrow line width (specified 303 MHz from the manufacturer, REO Inc., model R-33361).

The demonstrated contrast of 3.82×10^{-10} in Sec. 3 is broken down into its dominant effects based on these contrast values measured in various conditions. First, we observe the increase of the unmodulated light between (a) and (c) is 1.01×10^{-10} . We hypothesize this increase is due to two effects. One is the “occulter ghost” effect and the other is “chromatic residual”. Since the NKT laser has the shorter coherent length (less than 1 mm based on its laser linewidth) than the ghost path length (larger than 12.7 mm) while the HeNe has the longer coherent length (approximately 1.0 m based on its laser linewidth), the occulter ghost is expected to be coherent for (c), incoherent for (a). If coherent, it becomes modulated light. If incoherent, it becomes unmodulated light. Since the pairwise estimation scheme assumes the monochromatic light, any deviation from this assumption will go to the unmodulated light. Therefore, (a) will have more unmodulated light due to larger bandwidth. We name this contribution of unmodulated light “chromatic residual”.

The increase of 1.01×10^{-10} between (a) and (c) is in good agreement with our independent assessment of the occulter ghost effect of 1.07×10^{-10} in Sec. 4.2, implying that the occulter ghost effect is dominant among two effects. Therefore, we assign 1.01×10^{-10} as “occulter ghost” measurement in Table 1.

Second, we find the increase of the modulated light between (a) and (c) is 9.32×10^{-11} , which is caused by the increased control bandwidth. This is due to the limited capability of the WFC, thus, we name it as “chromatic control residual” measurement in Table 1. The chromatic control residual contribution can be further reduced by improvement of WFC algorithm and calibration accuracy. This value is compared to the theoretical model result of approximately 4×10^{-11} which is the DST design limit with ideal calibration (or perfect knowledge) and infinitely small DM actuator LSB.

Third, the smallest modulated light measured at the full dark hole is 8.78×10^{-11} in Fig. 4(c). Since this value is our controllable limit of contrast with the monochromatic light and agrees to the DM LSB effect assessment of 1×10^{-10} in Sec. 4.1, we regard this value as the “LSB effect of DM actuators” in Table 1.

Fourth, the smallest unmodulated light measured at the full dark hole is 9.23×10^{-11} in Fig. 4(c). We estimate some of this value is from the testbed LoS jitter. Our assessment of the “testbed LoS jitter” is 4.19×10^{-11} as

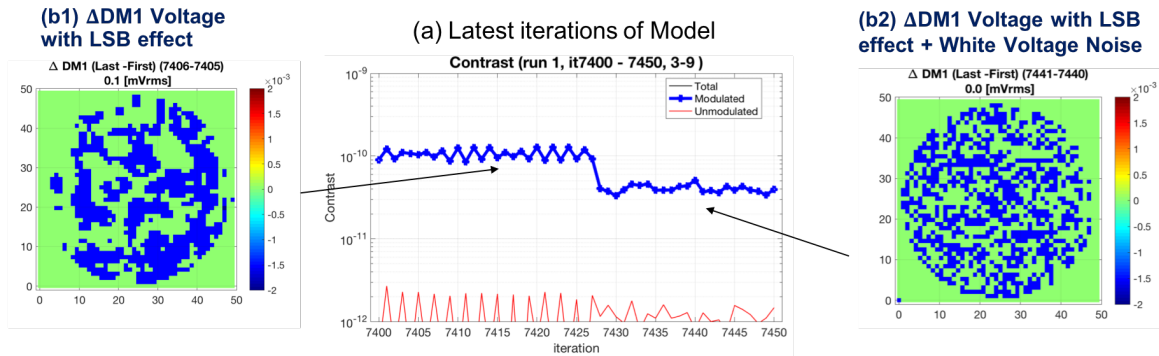


Figure 5. The latest iteration of a computer model simulation with the DM actuator LSB effect. We assume the applied voltage is quantized by its DM electronics LSB of 16 bit for 100 V range. Due to this LSB effect, the contrast is limited by approximately 1×10^{-10} as shown earlier part of iteration. See text for description of later iterations.

FALCO Model Result: Contrast vs. LSB

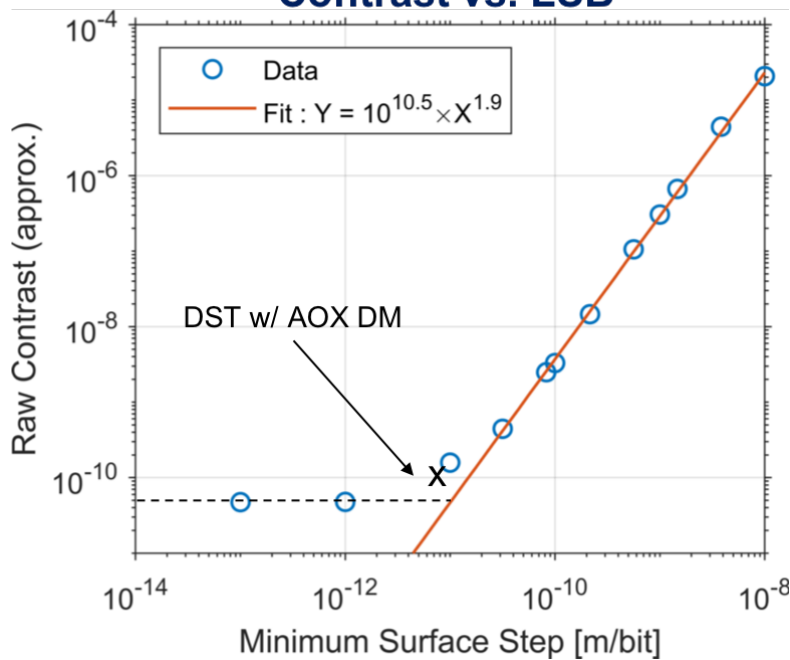


Figure 6. The raw contrast limit vs. the LSB of DM using another independent DST model (FALCO or Fast Linearized Coronaagraph Optimizer).

denoted in Table 1.* The residual of the unmodulated light of 5.04×10^{-11} is beyond our understanding as of 2019 and we assign this term as “unknown”.

4.1 LSB effect

We use compute models to estimate the DM LSB effect. Using on the testbed calibration, we build an in-situ testbed model. Because we use this model to compute the control matrix for the WFC for the testbed, we call this model “control model”.⁶

Fig. 5(a) shows the latest WFC iteration result when we run the control model itself as if we run the testbed. In running the control model, we assume the applied voltage is quantized by its DM electronics LSB of 16 bit

*DST LoS jitter impact is not described in this paper.

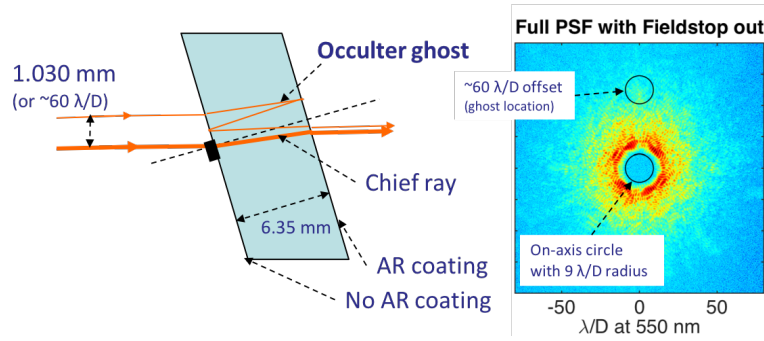


Figure 7. A sketch of DST occulter ghost path when the 6.35 mm thick fused silica substrate is used with AR coating only on the rear surface.

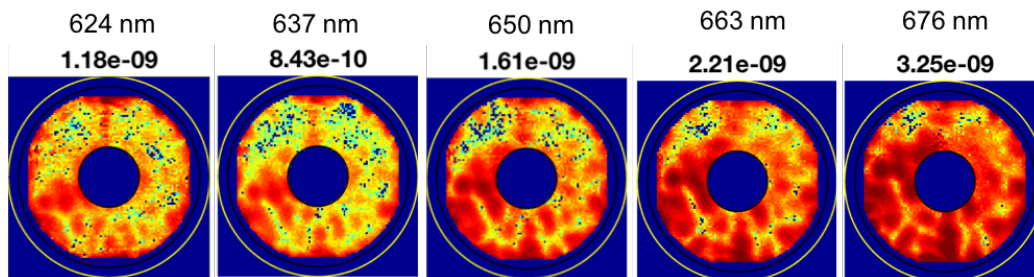


Figure 8. The testbed measurement of the unmodulated light at the higher wavelengths of 624 nm, 637 nm, 650 nm, 663 nm, and 676 nm. The occulter ghost is dominantly visible and morphologically marching to expected direction as the wavelength increases.

for 100 V range. Thus, its LSB is 1.5 mV corresponding approximately 6.0 pm surface considering 4nm/V DM actuator gain. The early (left) part of Fig. 5(a) shows the limit of the DM LSB effect is around 1×10^{-10} , which is the expectation value for the LSB effect denoted in Table 1. This value also agrees with the smallest modulated light measured at the full dark hole of 8.78×10^{-11} in Fig. 4(c).

White voltage noise can be added to the DM voltage to reduce the LSB effect as shown in the later (right) part of Fig. 5(a). However, this technique effect has not been observed in the testbed operation. This reason is not unknown.

In order to understand the DM LSB effect in more systematic way, we run another model by varying the LSB size. Shown in Fig. 6 is the raw contrast limit vs. the LSB of DM using an independent DST model (FALCO or Fast Linearized Coronagraph Optimizer).

As the minimum surface step decreases, the raw contrast obtained approaches its theoretical design contrast limit of approx. 5×10^{-11} . As the minimum surface step increases, the DM LSB effect becomes dominant and the contrast increases quadratically. DST has the minimum actuator step size of 6×10^{-12} m/bit. From this curve, the contrast limit due to the LSB effect is approximately 1.00×10^{-10} , reasonable agreement between two independent models.

4.2 Occluder ghost effect

The occulter ghost is caused by imperfect AR coating of the occulter substrate. As sketched in Fig. 7, the occulter ghost effect can be formulated in Eq. (1).

$$\text{Occluder ghost} = I \cdot R1 \cdot R2 \quad (1)$$

, where I is the measurable normalized intensity at around $62 \lambda/D$ (or around 1 mm) away from the chief ray, $R1$ and $R2$ are the front and rear reflection coefficients, and the transmission coefficients into/out-of the substrate are ignored.

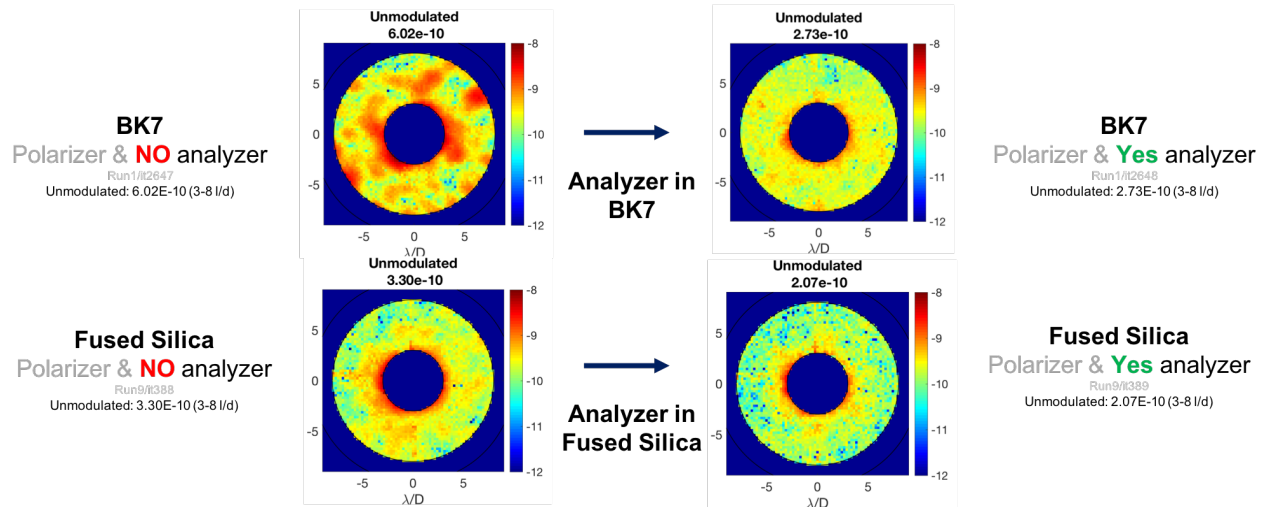


Figure 9. BK7 vs. fused silica. Two substrate materials are tested with and without the analyzer.

Fig. 8 shows the testbed measurement of the unmodulated light at higher wavelengths of 624 nm, 637 nm, 650 nm, 663 nm, and 676 nm. As shown in Fig. 8, the occulter ghost is dominantly visible and morphologically marching to the expected direction as the wavelength increases. Using the occulter ghost measurement (unmodulated light) of approximately 1.8×10^{-9} at 650 nm and the measure normalized intensity of 1.80×10^{-6} at $52 \lambda/D$ at 650 nm, the product of the reflection coefficients $R1 \cdot R2$ is computed as 1×10^{-3} at 650 nm.

According to vendors' AR coating specification, the reflection coefficients are $\times 10$ smaller at 550 nm comparing to 650 nm. Therefore, we can estimate the occulter ghost effect of 1.07×10^{-10} at 550 nm with the measure normalized intensity of 1.07×10^{-6} at $62 \lambda/D$ at 550 nm. This value is in the expectation of the occulter ghost effect in Table 1 and agrees to unmodulated light reduction when we use the long-coherent-length HeNe laser light source as described in earlier in this section.

4.3 Polarization effect from occulter substrates

Fig. 9 shows the unmodulated lights with and with polarization control with an analyzer in front of the image plane. The polarization effects are measured with unmodulated light decrease before and after the analyzer is inserted. They are 3.29×10^{-10} and 1.23×10^{-10} , respectively for BK7 and fused silica substrates. This relative ratio agrees to the birefringence measurement result as described in [9].

5. PLANET DETECTION CAPABILITY

Future space telescopes with high contrast imaging instruments will make use of post-processing algorithms, which maximize the planet searching and identification capability. To simulate such an observation and to characterize the realistic planet identification capability, we apply a post-processing algorithm to the testbed data as described below.

We first obtain a dark hole of around 4×10^{-10} raw contrast after WFC. Then, we continuously take the dark holes with 20 sec exposures, except for two subsequent WFC updates during 15 hours sequence. The 5 wavelength subbands of 528, 539, 550, 561, 572 nm are still used with 11 nm (2 %) bandwidth. Fig. 10 shows the "1 σ contrast noise" at $5 \lambda/D$ at a function of time. The 1 σ contrast noise is computed as the standard deviation of contrast values at the all pixels between $5 \lambda/D$ and $5 \lambda/D + 1$ pixel. The 1 σ contrast noise is our measure of the speckle noise when we apply the Angular Differential Imaging (ADI) technique for a post-processing algorithm later.

As shown in Fig. 10, the testbed appears to stabilize over time, i.e., the 1 σ contrast noise increase rate decreases for later measurement. Whereas in the first sequence takes 3 hr to approach 1×10^{-9} , the third sequence degrades by same amount in 5 hr. Based on our previous experiment, we believe that the contrast noise degradation is largely due to the employed DM (Xinetics 48x48)'s thermal sensitivity with an additional

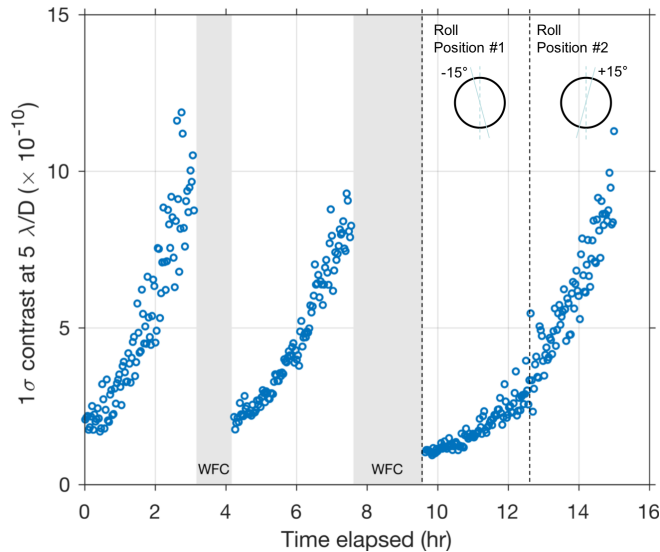


Figure 10. Testbed drift. We continuously take the dark holes with 20sec exposures, except for two subsequent WFC updates during 15hours sequence. The plot is the “ 1σ contrast noise” at $5 \lambda/D$ as a function of time. The 1σ contrast noise is computed as the standard deviation of contrast values at the all pixels between $5 \lambda/D$ and $5 \lambda/D + 1$ pixel. The 1σ contrast noise is our measure of the speckle noise when we apply the Angular Differential Imaging (ADI) technique for a post-processing algorithm in Fig. 11.

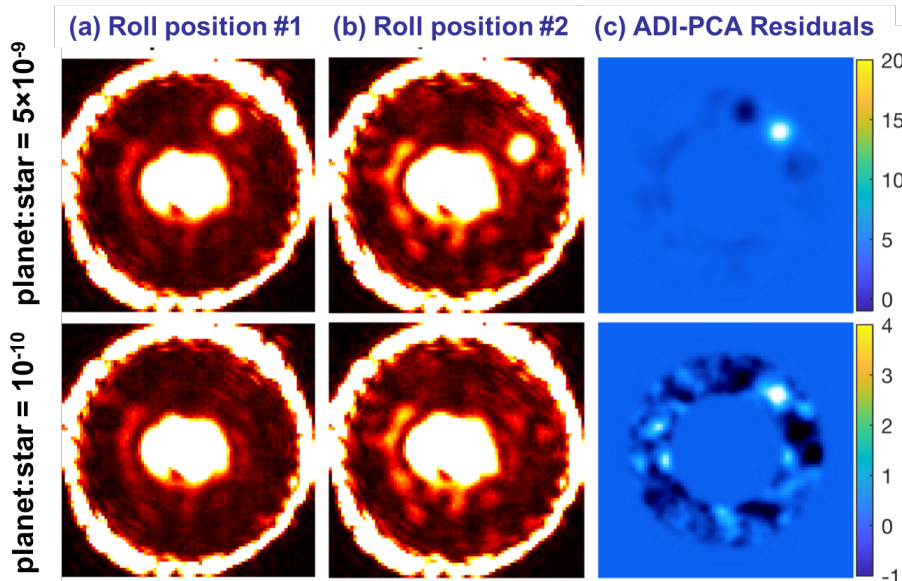


Figure 11. The averaged contrast images at the roll position #1 (a) and #2 (b) in Fig. 10. A numerically generated planet is injected for demonstration purpose. We perform the ADI simulation to obtain a differential image shown in (c). The upper and lower parts are same simulation except the planet brightness of 5×10^{-9} and 1×10^{-10} is considered respectively. This demonstrates that a 1×10^{-10} planet imaging is feasible with 4σ contrast noise level after ADI is applied in DST.

irregular external disturbance contributing to the earlier drift in the sequence. However, no experiment to prove our hypothesis has been done.

We utilize these testbed data to simulate a simple ADI. We assume a 30 degree roll near middle of the last sequence as indicated in the last sequence of Fig. 10. We also assume a planet at the $5 \lambda/D$ with a certain brightness. In generating a planet, we numerically convolve a point with measured the Point Spread

Function (PSF). Fig. 11(a) and Fig. 11(b) are the averaged contrast images at the roll position #1 and #2 respectively with the numerically generated planet. Then, we perform the ADI simulation using the VIP package[†] to obtain differential image shown in Fig. 11(c). The upper and lower parts in Fig. 11 are same simulation except the planet brightness of 5×10^{-9} and 1×10^{-10} is considered respectively.

As a result, the 1σ contrast noise floor is measured as 2.5×10^{-11} at $5 \lambda/D$. This implies that a 1×10^{-10} planet imaging is feasible with 4σ contrast noise level as we can see in the bottom of Fig. ??(c) when we numerically inject the 1×10^{-10} planet.

6. CONCLUSION

We have demonstrated reaching starlight suppression 3.82×10^{-10} averaged across the $3 \lambda/D$ and $8 \lambda/D$ 360 degree dark hole using the 10 % broadband light at 550 nm. To the best of our knowledge, this raw contrast is the highest 10% contrast ever achieved in the testbed environment. Furthermore, we could understand the current contrast limit, key contributions and unknowns using testbed measurement and model analysis.

We also find that DST can achieve coronagraph contrast performance capable of detecting a planet as dim as 1×10^{-10} (4σ level) at $5 \lambda/D$ after using a standard (or conventional) post-processing technique.

For next few years, DST will be utilized to demonstrate various key technological aspects of future coronagraph missions¹⁰ including different DM technology, low and mid-order Wavefront Sensor (WFS), and segmented pupil obscuration. The result from DST is expected to be valuable and support the future coronagraph missions such as LUVOIR and HabEx.

ACKNOWLEDGMENTS

This work was carried out at the Jet Propulsion Laboratory, California Institute of Technology, under contract with the National Aeronautics and Space Administration (NASA). We would like to acknowledge funding from NASA's Exoplanet Exploration Program Office, in addition to contributions small and large from the broader WFIRST-CGI, HCIT, and MDL teams.

REFERENCES

1. The LUVOIR Team, "The Large UV Optical Infrared Surveyor (LUVOIR) final report." https://asd.gsfc.nasa.gov/luvoir/resources/docs/LUVOIR_FinalReport_2019-08-26.pdf, 2019.
2. The HabEx Team, "Habitable Exoplanet Observatory Final Report." <https://www.jpl.nasa.gov/habex/pdf/HabEx-Final-Report-Public-Release.pdf>, 2019.
3. W. A. Traub, R. Belikov, O. Guyon, N. J. Kasdin, J. Krist, B. Macintosh, B. Mennesson, D. Savransky, M. Shao, E. Serabyn, and J. Trauger, "Science yield estimation for AFTA coronagraphs," in *Society of Photo-Optical Instrumentation Engineers (SPIE) Conference Series, Society of Photo-Optical Instrumentation Engineers (SPIE) Conference Series* **9143**, p. 0, Aug. 2014.
4. K. Patterson, B.-J. Seo, K. Balasubramanian, T. Chui, B. Crill, J. Gill, B. D. Kern, R. Lam, D. Marx, D. Moody, R. Muller, C. M. Prada, G. Ruane, J. Shaw, F. Shi, N. Siegler, H. Tang, J. Trauger, V. White, D. W. Wilson, K. Yee, and R. Zimmer, "Design description and commissioning performance of a stable coronagraph technology development testbed for direct imaging of Earth-like exoplanets," *Proc. SPIE* **11117**, p. 111171U, 2019.
5. J. T. Trauger and W. A. Traub, "A laboratory demonstration of the capability to image an Earth-like extrasolar planet," *Nature* **446**, pp. 771–773, Apr. 2007.
6. B.-J. Seo, E. Cady, B. Gordon, B. Kern, R. Lam, D. Marx, D. Moody, R. Muller, K. Patterson, I. Poberezhskiy, C. M. Prada, E. Sidick, F. Shi, J. Trauger, and D. Wilson, "Hybrid lyot coronagraph for wfirst: high-contrast broadband testbed demonstration,"
7. B.-J. Seo, B. Gordon, B. Kern, A. Kuhnert, D. Moody, R. Muller, I. Poberezhskiy, J. Trauger, and D. Wilson, "Hybrid Lyot Coronagraph for WFIRST-AFTA: Occulter Fabrication and High Contrast Narrowband Testbed Demonstration," 2015.

[†]<https://github.com/vortex-exoplanet/VIP>

8. A. Give'on, B. D. Kern, and S. Shaklan, "Pair-wise, deformable mirror, image plane-based diversity electric field estimation for high contrast coronagraph," **8151**, 2011.
9. K. Balasubramanian, B.-J. Seo, K. Patterson, C. M. Prada, A. J. E. Riggs, H. Zhou, D. Moody, E. Cady, V. White, K. Yee, R. Muller, P. Echternach, F. Greer, and D. Wilson, "Critical characteristics of coronagraph masks influencing high contrast performance," *Proc. SPIE* **11117-63**, 2019.
10. G. Ruane, B. Crill, K. Patterson, C. M. Prada, B.-J. Seo, and N. Siegler, "Decadal survey testbed commissioning roadmap: Demonstrating technology for imaging new worlds." https://exoplanets.nasa.gov/internal_resources/1170/, 2019.